APPLIED SCIENCES AND ENGINEERING

Why are soft collagenous tissues so tough?

Jingyuan Tang[1], Xi Chen[1], Fengkai Liu[1], Liangsong Zeng[1]†, Zhigang Suo[2]*, Jingda Tang[1]*

Bovine pericardium is the tissue of choice for replacing heart valves of human patients in minimally invasive surgery. The tissue has an extraordinarily high toughness of ~100 kilojoules per square meter. Here, we investigate the origin of the toughness through mechanical tests and microscopic observations. In the tissue, crimped, long, strong collagen fibers are embedded in a soft matrix. As a crack grows in the matrix, the fibers decrimp, reorient, slip, and bridge the crack. These microscopic processes enable the fibers to transmit high tension over a long distance. Using two types of experiments, we measure the bridging traction as a function of crack separation, $\sigma(\delta)$. The peak traction is σ_0 ~ 60 megapascals. The maximum separation is δ_0 ~ 6 millimeters, two to four orders of magnitude higher than that of hard tissues. Both the high traction and large separation of the bovine pericardium contribute to its high toughness.

INTRODUCTION

Soft collagenous tissues, such as skin, tendon, fetal membrane, and heart valve, have high toughness (*1*–*4*). For example, during amniocentesis, a human fetal membrane is punctured by a needle with a diameter of ~1 mm but resists rupture and prevents miscarriage (*5*). As another example, bovine pericardium (BP) membrane, harvested from the bovine heart, has been used to replace heart valves of human patients (Fig. 1A). The replaced heart valve resists crack growth after hundreds of millions of cycles (*6*, *7*).

This paper investigates the origin of the high toughness of the BP membrane using a combination of mechanical tests and microscopic observations. This study has become urgently needed. When used in human patients, BP has a limited service time of less than 10 years due to calcification, necessitating repeated surgeries (*8*). Efforts have been made worldwide to develop synthetic polymers to substitute BP, but such efforts have been unsuccessful because these synthetic substitutes grow cracks (*9*).

The BP membrane used in this work has a thickness of ~300 μm (Fig. 1B). Multiphoton microscope images show the collagen fiber network (Fig. 1C) and elastin fiber network (Fig. 1D). In the membrane, the collagen fibers are crimped and form a network, embedded in a matrix of elastin and proteoglycan (*10*) (Fig. 1E). The collagen has a hierarchical structure (Fig. 1F). Three polypeptide chains form a triple helix by hydrogen bonds and covalent bonds, called the tropocollagen (*11*). The length of a tropocollagen is ~300 nm. The tropocollagen helices are staggered and cross-linked by covalent bonds to form a collagen fibril (*12*, *13*). A collagen fibril has a length of 0.5~10 mm and a diameter of 50~500 nm (*14*–*17*). The fibrils form collagen fibers of a diameter of 10~50 μm and a length of ~10 mm. The strength of a collagen fiber is 30~200 MPa (*18*–*20*). The collagen fibers are interconnected by elastin, proteoglycan, and small diameter fibrils (*3*). The elastin fibers have a modulus of 300~600 kPa, and the elastin network has a low toughness of 20 J/m^2 (*21*). The crimped collagen fibers enable softness at small to moderate stretches but high resistance to crack growth at a large stretch (*3*). Elastin enables high elasticity of the collagen network at small deformation (*22*). The proteoglycan keeps the tissue hydrated and separates the fibrils to allow them to slip (*23*).

When crack grows in the soft collagenous tissue, collagen fibers recruit and form a bridging zone at the crack tip to hinder the crack growth (*1*, *2*, *5*, *24*–*26*). Crack bridging is characterized by a traction-separation curve (*27*). Traction-separation curves have been used to describe crack growth in various materials, as well as adhesion between dissimilar materials (*28*–*34*). In this work, we aim to measure the traction-separation curve of BP to reveal the toughening mechanism, which will help the development of biomimetic materials.

This paper investigates the origin of the high toughness of BP through mechanical tests and microscopic observations. We measure the traction-separation curve of BP using two methods. In the first method, a sample is cut from two edges, leaving a ligament containing a small number of collagen fibers. We pull the sample and measure the traction-separation curve. Slip between the fibers is observed. In the second method, a sample is cut with a long crack. We pull the sample and observe the crack growth. When a crack impinges upon a collagen fiber, the surrounding soft and weak matrix enables the fiber to decrimp, reorient, and slip. As the crack grows, the collagen fibers pull out from the matrix and bridge the crack surfaces (Fig. 2). Two values of energy release rate are identified, G_A and G_B. The precut crack starts to grow at G_A, when the fibers decrimp and reorient. As crack grows, the fibers are pulled out from the matrix and bridge the crack surfaces. At G_B, multiple cracks are observed far away from the precut crack tip. We measure the energy release rate as a function of crack separation and convert this function to the traction-separation curve $\sigma(\delta)$. The two methods give comparable traction-separation curves. The peak traction of BP is σ_0 ~ 60 MPa, close to that of hard tissues (e.g., fish scale and bone). The maximum separation of BP is δ_0 ~ 6 mm, two to four orders of magnitude higher than that of hard tissues. We further investigate how traction-separation curves vary with samples with different fiber orientations and dehydration. It is hoped that this investigation will aid the development of synthetic materials of high crack resistance.

RESULTS

Fiber pullout experiment

We prepare a rectangular membrane with a width of 10 mm and a height of 30 mm. The sample is cut from two edges in the middle

---

[1] State Key Laboratory for Strength and Vibration of Mechanical Structures, Department of Engineering Mechanics, Xi'an Jiaotong University, Xi'an 710049, China. [2] John A. Paulson School of Engineering and Applied Sciences, Harvard University, Cambridge, MA, USA.
*Corresponding author. Email: suo@seas.harvard.edu (Z.S.); tangjd@mail.xjtu.edu.cn (J.T.)
†Present address: Department of Mechanical Engineering, Northwestern University, Evanston, IL, USA.

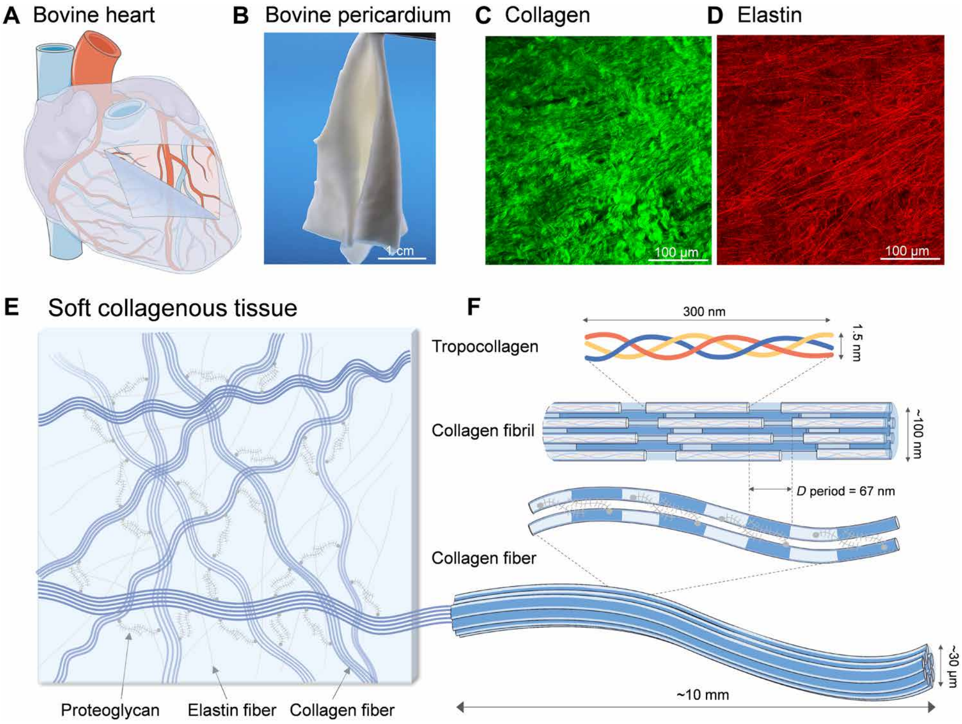

Fig. 1. Structure of bovine pericardium (BP). (**A**) BP membrane is harvested from the bovine heart. (The figure is partly created using Servier Medical Art, licensed under Creative Commons Attribution 4.0 International. https://creativecommons.org/licenses/by/4.0/) (**B**) Photo of a BP membrane. The multiphoton images of the (**C**) collagen fiber network and (**D**) elastin fiber network. (**E**) Schematic of a network of collagen fibers embedded in a matrix of elastin and proteoglycan. (**F**) Hierarchical structure of collagen: tropocollagen, fibril, and fiber.

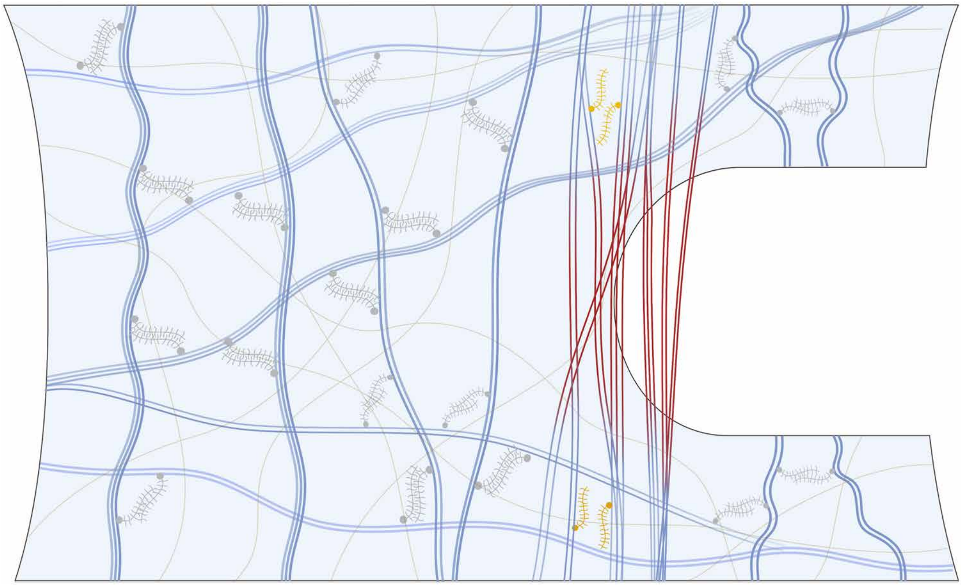

Fig. 2. Collagen fibers bridge a crack growing in the soft matrix. When the crack grows in the soft matrix, the collagen fibers decrimp, reorient, and slip, bridging the crack.

plane, leaving a ligament of a width of ~300 μm, with a small number of collagen fibers (Fig. 3A). The upper and lower edges of the sample are glued between acrylic sheets. The edges are gripped by a tensile tester and are pulled, whereas the pullout of the fibers is recorded by a video camera (Fig. 3B). Before the test, the upper and lower parts of the sample are connected only by the ligament. As the upper grip displaces, the ligament begins to pull out. Because of the multilayered structure of the membrane and the dispersion of fiber orientation, the ligament delaminates. As the displacement increases, most of the short fibers are completely pulled out, leaving only a thin fiber, ~80 μm in width, connecting the upper and lower parts of the sample.

We record the force-displacement curves of the samples (Fig. 3C). Because the entire specimen undergoes elastic deformation during the pullout, we remove the elastic deformation from the total displacement to obtain the separation δ_t (Fig. 3D and fig. S1). The traction σ is obtained by dividing the force by the cross-sectional area in the undeformed state. When the fibers begin to be pulled out, the traction increases sharply, peaks at ~53 MPa, and then decreases. After ~6 mm of pullout, the traction becomes negligible.

To investigate the microscopic process of fiber pullout, polarized light microscope images are captured during the pullout process of ligaments (Fig. 4A). Before conducting the pullout test, microscope images are taken to measure the initial width of each ligament (Fig. 4A, I). As the pullout begins, the upper and lower parts of the specimen deform along the pullout direction, and the fibers within the ligament begin to decrimp. The ligament is then steadily pulled out, with the uncrimped fibers slipping out of the lower part of the specimen (Fig. 4A, II). The membrane has multiple layers of fibers in different orientations. As the ligament is pulled, the membrane delaminates (Fig. 4A, III). Last, the ligament with a total length of ~10 mm is completely pulled out (Fig. 4A, IV). Such a long pullout length results from the long initial length and recruitment of collagen fibers. Microscopic observation of the complete fiber pullout process is shown in movie S1. The pullout behavior of collagen fibers depends on the loading speed because the interfiber sliding is related to the loading speed (*35*, *36*). When the fiber is pulled out at a lower speed of 2 mm/min, the peak traction is lower than that of samples loaded at 20 mm/min, and the fiber pullout length is higher. When the fiber is pulled out at a higher loading speed of 200 mm/min, the peak traction is higher than that of samples loaded at 20 mm/min, but the fiber pullout length becomes lower (fig. S3).

To further study the microstructural change of the fibers, multiphoton images are taken (Fig. 4B). Before the pullout test, the crimped collagen fibers are embedded in the elastin networks (Fig. 4B, I). As the pullout begins, the fibers decrimp and reorient. The pullout of the ligament also affects the surrounding fibers to reorient along the pullout direction (Fig. 4B, II). As the long fibers are pulled out, elastin can be observed on the fibers (Fig. 4B, III). Images are taken every 5 μm along the thickness direction of each sample. The three-dimensional (3D) morphology of the pullout sample is shown in fig. S2. The morphology of collagen fibers in

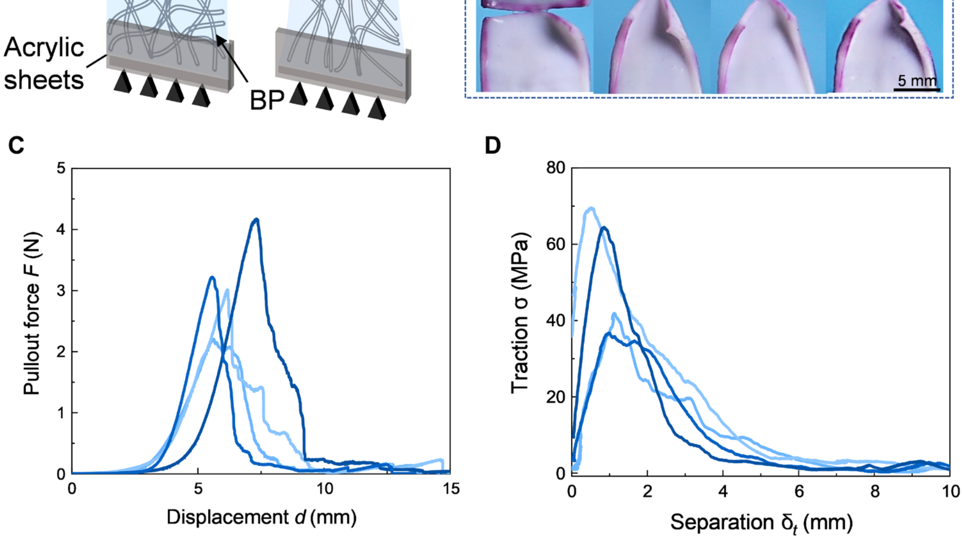

Fig. 3. Pull out a small number of fibers from a membrane. (**A**) A sample is cut from two edges, leaving a ligament of a width of ~300 μm, with a small number of collagen fibers. The sample is then pulled. (**B**) Four snapshots of the sample. (**C**) Pullout force-displacement curves of several samples. (**D**) Traction-separation curves, $\sigma(\delta_t)$. The number of samples, $n = 4$.

different layers of the sample along the thickness direction is shown in movies S2 and S3.

Crack growth experiment

We then examine crack growth in membranes. We precut a crack in a membrane, stretch the membrane and observe the crack tip using the polarized light microscope and scanning electron microscope. In the undeformed sample, the crack tip remains intact, and the fibers are crimped (Fig. 5A). Upon stretching, the crack initially blunts rather than grows. The crimped fibers straighten and reorient along the stretching direction (Fig. 5B). Upon further stretching, the crack grows in the matrix, and the fibers pull out and bridge the crack (Fig. 5C).

The crack growth experiment also enables us to determine the traction-separation curve σ(δ). A rectangular sample with a precut

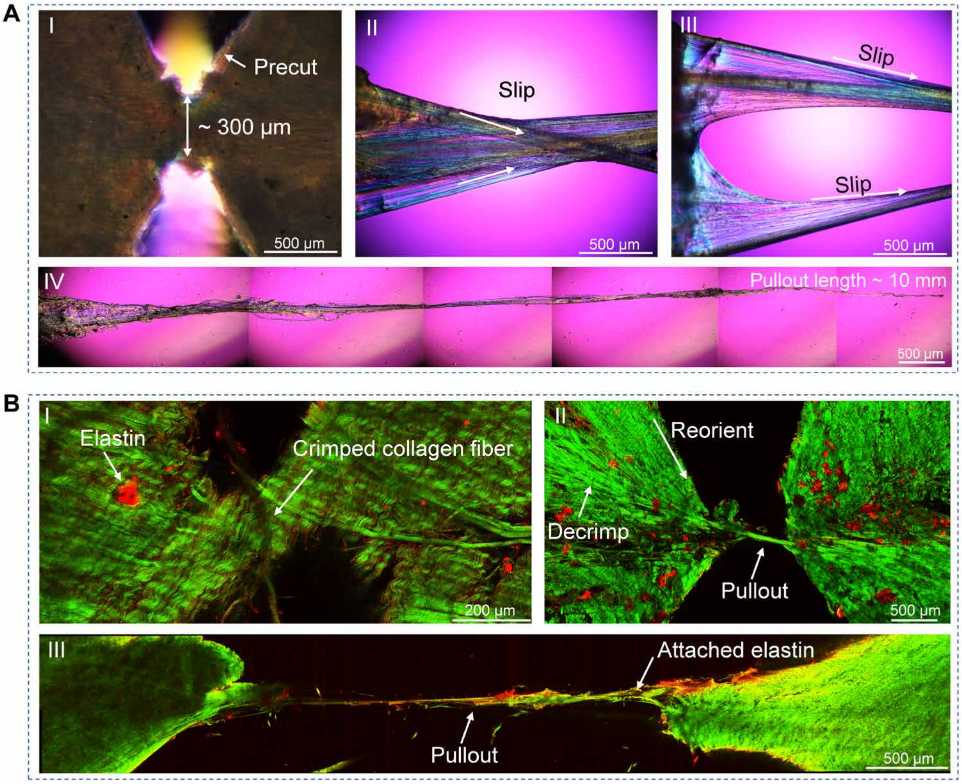

Fig. 4. Snapshots of fiber pullout. (**A**) Polarized light microscope images I, II, III, and IV are taken from the same sample. (**B**) Multiphoton images I, II, and III are taken from three different samples. Collagen fibers are shown in green, and elastin is shown in red.

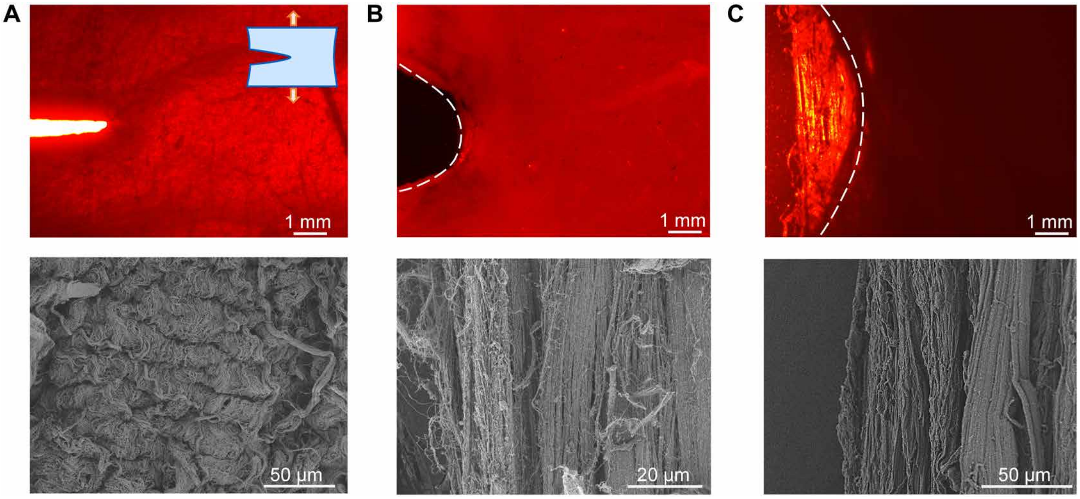

Fig. 5. Images of a crack tip in the polarized light microscope and scanning electron microscope. (**A**) An undeformed sample contains a precut crack. (**B**) When the sample is stretched, the crack blunts, and the fibers at the crack tip decrimp and reorient to the stretching direction. (**C**) As the crack grows in the matrix, the fibers bridge the crack.

crack is prepared, clamped along its two long edges, stretched, and observed in a video camera. The sample has an initial height of H (Fig. 6A). When the sample is stretched to the current height of h, the stretch is defined by $\lambda = h/H$ (Fig. 6B). Let $W(\lambda)$ be the energy per volume stored in uncracked samples. The energy release rate is given by (*37*)

$$G = HW(\lambda) \tag{1}$$

To convert the stretch to the energy release rate, we calculate W using the area under the stress-stretch curve of the precut sample, considering the large statistical variability in soft collagenous tissues.

From the video, we take several snapshots, in which we identify two values of energy release rate: G_A and G_B (Fig. 6C). The surface of the precut crack is inked, and the membrane is then stretched. When $G < G_A$, the crack blunts, and the inked surface remains continuous, whereas the fibers reorient and decrimp. When $G = G_A$, the ink breaks, and the crack starts to grow in the matrix. When $G_A < G < G_B$, the crack surfaces separate by a displacement δ_t, and the fibers pull out and bridge the crack with a traction, σ. Both δ_t and σ vary from point to point along the crack. The bridging traction is a function of the crack separation, $\sigma(\delta_t)$. Denote the distance between the crack surfaces at the tail by δ_t. In the experiment, as G increases, δ_t also increases and is recorded, giving the function $G(\delta_t)$. On the basis of the assumption of small scale bridging, the two functions, $\sigma(\delta)$ and $G(\delta_t)$, are related by (*38*)

$$G(\delta_t) = G_A + \int_o^{\delta_t} \sigma(\delta)d\delta \tag{2}$$

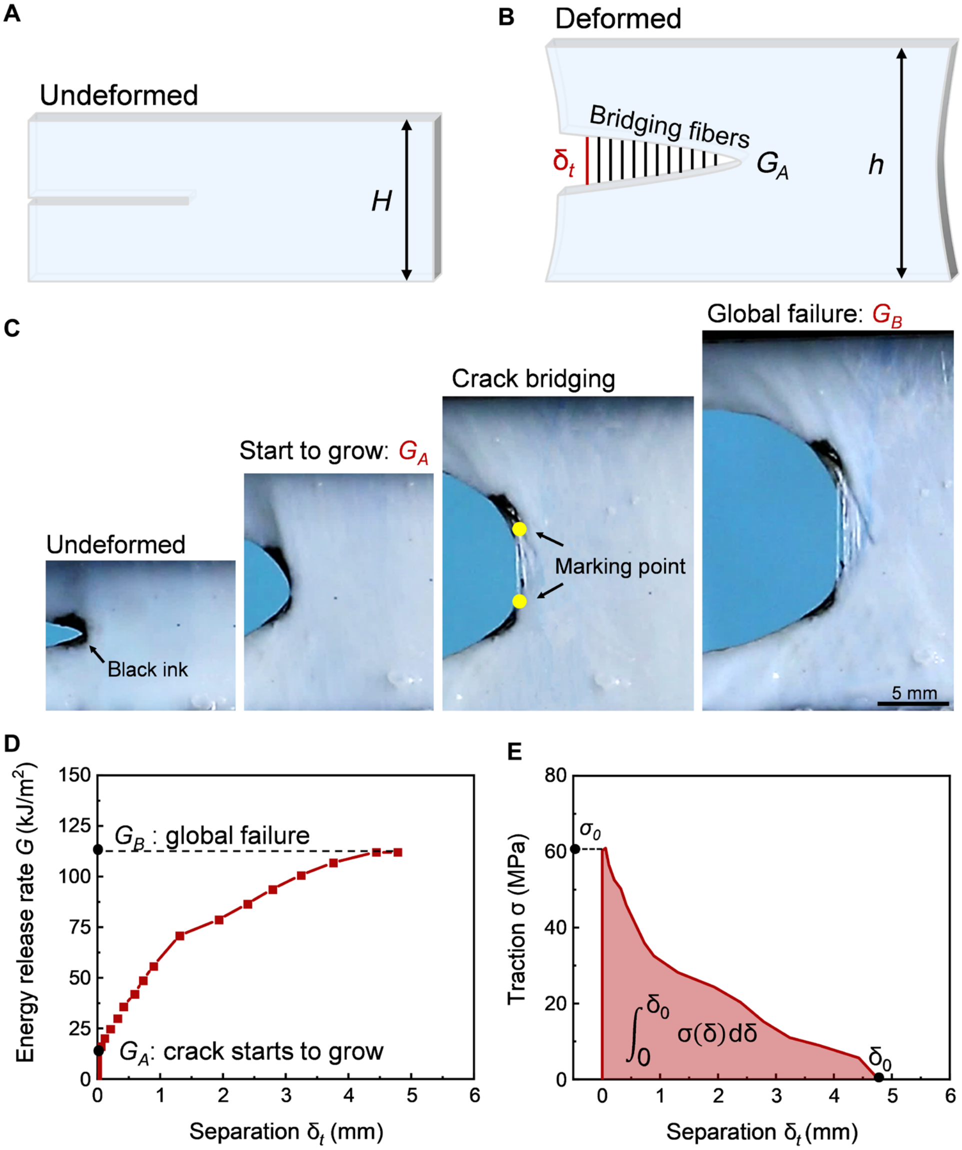

Fig. 6. Experiment of crack growth. (**A**) Cut a long rectangular sample from a membrane, cut the sample with a crack, and ink the surface of the crack. (**B**) When the sample is stretched, the crack grows in the matrix, and the fibers bridge the crack. The distance between the broken ends of the ink defines the separation at the tail of the crack, δ_t. (**C**) Snapshots of the crack. (**D**) The energy release rate G is a function of crack separation δ_t. (**E**) Traction-separation curve, $\sigma(\delta_t)$.

Differentiating the above equation with respect to δ_t, we obtain that

$$\frac{dG(\delta_t)}{d\delta_t} = \sigma(\delta_t) \tag{3}$$

This equation can be used to determine the function $\sigma(\delta_t)$ from the experimentally measured function $G(\delta_t)$ (*30*). When $G = G_B$, the sample starts to fail globally, with multiple cracks observed far away from the precut crack tip.

We measure δ_t by the distance between the two ends of the broken ink, measure G by Eq. 1, and plot the experimentally obtained function $G(\delta_t)$ (Fig. 6D). The separation of the crack at the tail, δ_t, is recorded using a camera with a resolution of ~10 μm. This resolution sets a limit on what we can determine when the inked surface breaks. We fit the initial portion of the recorded G-δ_t curve by a quadratic polynomial and extrapolate the energy release rate G_A at which the crack growth initiates. This procedure gives $G_A = 16.2$ kJ/m^2. Our experiment records that $G_B = 112.1$ kJ/m^2. According to Eq. 3, the traction-separation curve is determined by differentiating G with respect to δ_t (Fig. 6E). When the crack begins to open, the traction sharply reaches the peak of $\sigma_0 \sim 60.9$ MPa at a small separation of 60 μm. As the separation further increases, the traction gradually decreases, until the sample fails globally at a maximum separation of $\delta_0 \sim 4.8$ mm. The pullout behavior of collagen fibers at the crack tip is related to the loading speed (fig. S4). When the loading speed is 2 mm/min, the collagen fibers at the crack tip pull out steadily. When the loading speed is 200 mm/min, the fiber pullout events reduce obviously, and global failure of the sample occurs quickly.

Effect of sample height on the traction-separation curve

The traction-separation curve has been used as a material property to evaluate the toughness and bridging zone size. It is necessary to verify whether the measured traction-separation curve is independent of the sample geometry. We change the sample height and conduct the crack growth experiment. When the sample height $H > 5$ mm, all the samples undergo the sequential processes of crack bridging and global failure (fig. S5). The function $G(\delta_t)$ is indistinguishable for various sample heights (Fig. 7A). For the sample with a height of 5 mm, G reaches G_B at a very small crack separation δ_t because the sample undergoes global failure quickly instead of forming a bridging zone after crack growth. Thus, the measurements of δ_t and G will stop prematurely. We obtain G_A for various sample heights (Fig. 7B). When $H > 5$ mm, G_A almost does not

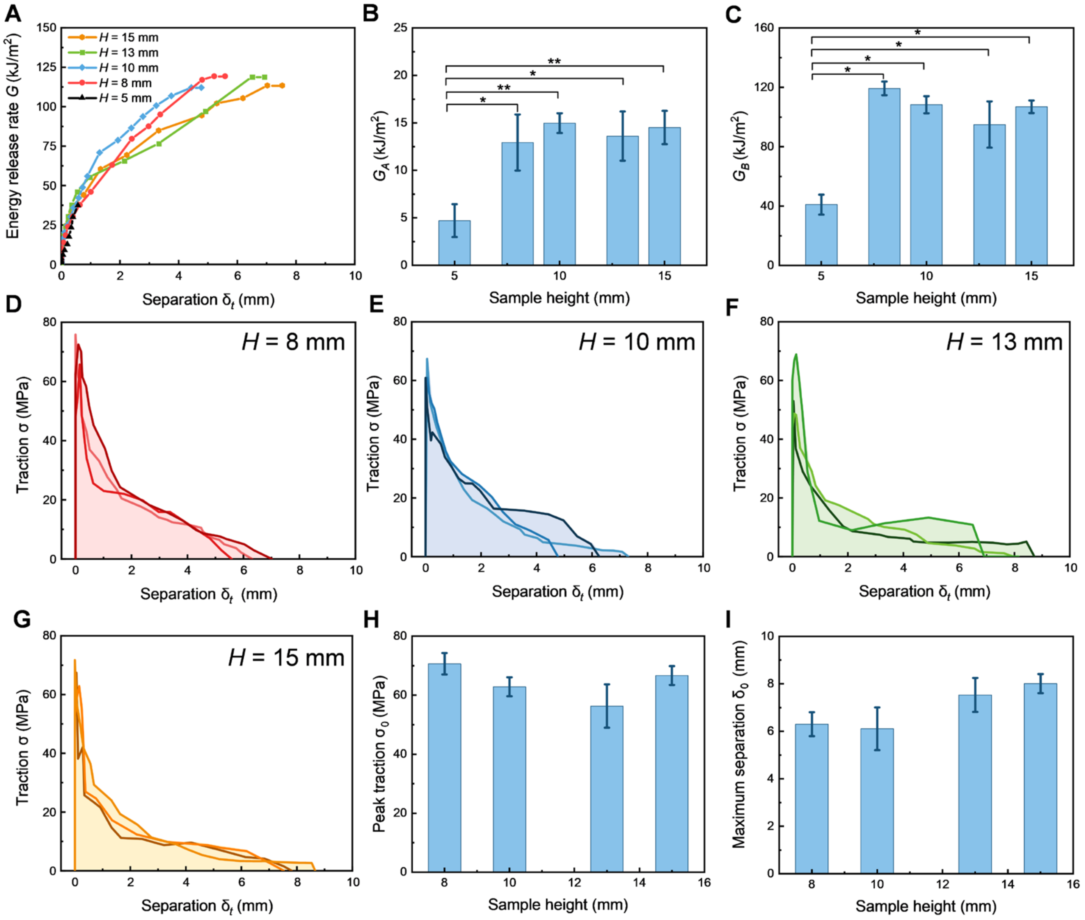

Fig. 7. Crack growth experiments with samples of various heights. (**A**) Energy release rate G as a function of the crack separation δ_t. (**B**) Energy release rate at crack growth initiation, G_A, and (**C**) the energy release rate at global failure, G_B. The traction-separation curves of samples with various heights of (**D**) 8 mm, (**E**) 10 mm, (**F**) 13 mm, and (**G**) 15 mm. (**H**) Peak bridging traction σ_0 and (**I**) the maximum crack separation δ_0 change negligibly with the sample height. The number of samples, $n = 3$, for all heights. Significant differences ($P < 0.05$) are indicated by the Kruskal-Wallis test.

change with the sample height, reaching a plateau of ~13.2 kJ/m^2. When $H = 5$ mm, G_A of the sample is lower than that of higher samples. This is because the small sample height limits a region at the crack tip, within which fibers decrimp and reorient. We then obtain G_B of samples with various heights (Fig. 7C). When $H > 8$ mm, G_B reaches a plateau of ~107.3 kJ/m^2, also higher than that of samples with height of 5 mm. We further investigate the effect of initial crack length on the crack propagation process of samples (fig. S6). For the sample height of $H = 5$ mm, the samples undergo global failure quickly, no matter the initial crack length is 10 or 20 mm. For the sample height of $H = 10$ mm, the samples undergo crack bridging and global failure in sequence, no matter the initial crack length is 10 or 20 mm.

The traction-separation curves for various sample heights show the same trend (Fig. 7, D to G). The traction increases sharply to the peak and gradually decreases with a large crack separation. Both the peak traction σ_0 and the maximum separation δ_0 are compared (Fig. 7, H and I). The average σ_0 is ~64.1 MPa, and the average δ_0 is ~6.9 mm. The results confirm that the traction-separation curve obtained by the crack growth experiment is independent of the sample height. When $H = 5$ mm, it is difficult to observe the complete bridging process, so the traction-separation curves are not calculated.

Effect of fiber orientation on the traction-separation curve

The distribution of fibers in any given BP membrane is usually uneven, with fibers highly aligned in some regions and not aligned in other regions (*39*). We use the small-angle light scattering (SALS) test to detect the fiber orientation in the membrane (fig. S7, A and B). Samples are divided into three categories (*40*, *41*). The samples in which fibers are not aligned are called highly dispersed (HD) samples. Of samples in which fibers are highly aligned, those loaded in the direction perpendicular to the fibers are called crossfiber-direction (XD) samples, and those loaded in the direction parallel to the loading direction are called preferred-direction (PD) samples (Fig. 8A).

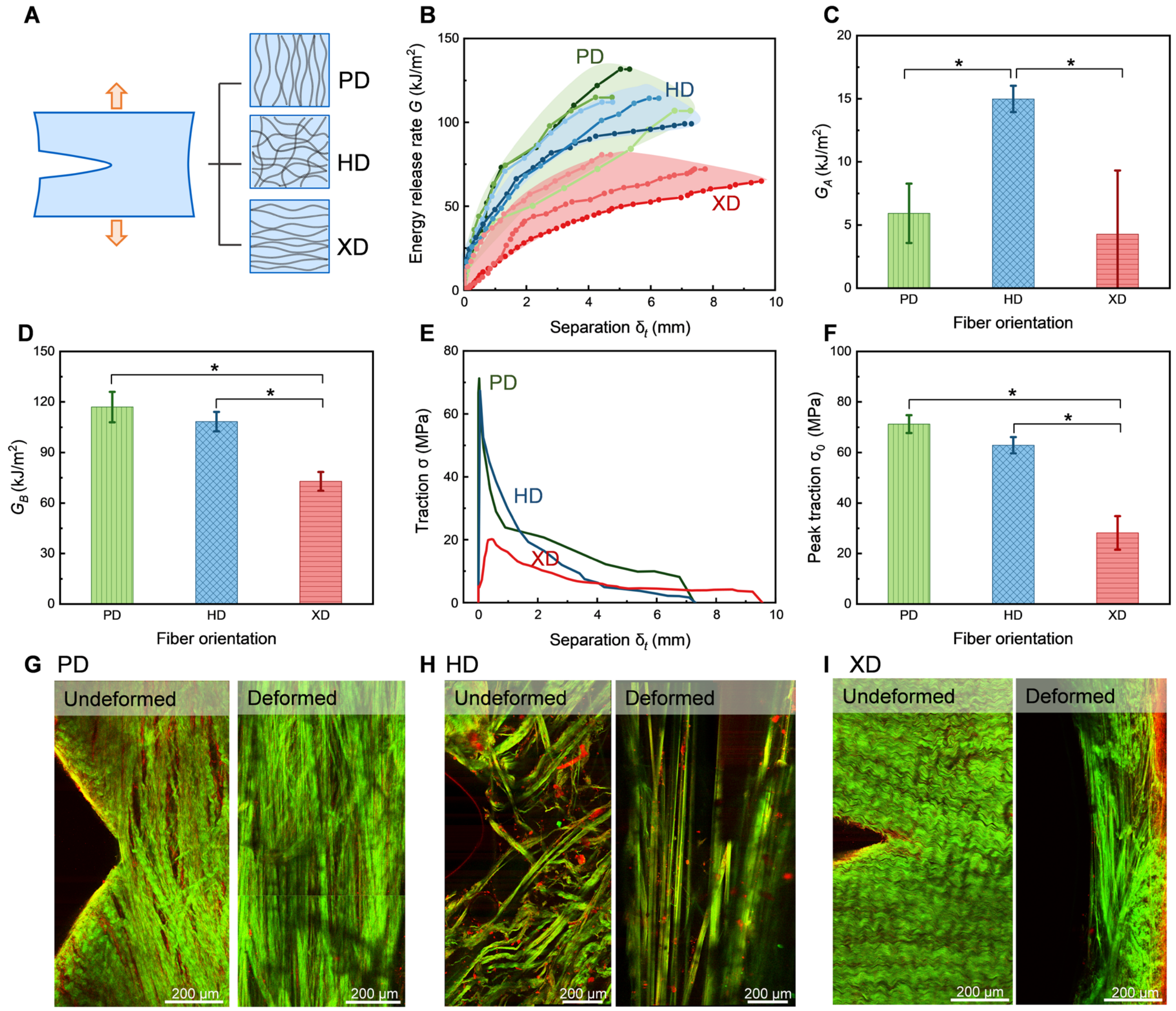

Fig. 8. Crack growth experiments using samples with various fiber orientations. (**A**) The membrane is divided into three groups depending on the relation between the loading direction and fiber aligned direction. (**B**) Energy release rate G as a function of the crack separation δ_t. (**C**) Energy release rate at crack growth initiation, G_A. (**D**) Energy release rate at global failure, G_B. (**E**) Traction-separation curves and (**F**) the peak traction σ_0 of samples with various fiber orientations. The multiphoton images at the crack tip of the (**G**) PD sample, (**H**) HD sample, and (**I**) XD sample in the undeformed state and deformed state. The sample height is fixed at 10 mm for all the tests. The number of samples, $n = 3$, for HD, XD, and PD groups. Significant differences ($P < 0.05$) are indicated by the Kruskal-Wallis test.

We conduct the crack growth experiment to measure the traction-separation curves of the three groups of samples. The stress-stretch curves show that PD samples have the highest maximum stress and modulus among three groups, whereas the XD samples have the lowest values (fig. S7C). We also measure the function $G(\delta_t)$ for the three groups of samples (Fig. 8B). Note that G_A is 5.9, 14.9, and 4.2 kJ/m^2 for PD, HD, and XD samples, respectively (Fig. 8C). For XD samples, scanning electron microscope images show that, when the crack starts to grow, most of the fibers still align perpendicularly to the stretch direction and do not bear load. Only a few fibers reorient and decrimp (fig. S8A). In contrast, for both PD and HD samples, all fibers are aligned along the stretch direction when crack starts to grow (fig. S9A). For PD samples, the fibers are initially aligned along the stretching direction. When the crack opens, G_A originates only from fiber decrimp. For HD samples, nearly all fibers reorient and decrimp during stretch, leading to the highest G_A. We then determine G_B of three groups of samples and find that G_B of the XD sample is notably lower than that of other two groups (Fig. 8D).

The fiber orientation also influences the crack bridging behavior. We determine the traction-separation curves of the three groups of samples. We plot one traction-separation curve from each of the three groups of samples (Fig. 8E) and show the repetitive results in fig. S10. We compare the peak traction σ_0 (Fig. 8F). Both HD and PD samples have similar values of σ_0, which are higher than that of XD samples. Multiphoton images and scanning electron microscope images are taken for the crack tips in the undeformed state and deformed state. For PD samples, the fibers are crimped and align along the loading direction in the undeformed state. After the crack growth, the fibers are densely arranged in the bridging zone (Fig. 8G and fig. S9B). For HD samples, the 2D and 3D multiphoton images show that fibers do not align in the undeformed state. However, in the deformed state, all fibers reorient along the stretch direction and contribute to bridging the crack (Fig. 8H and fig. S11). In contrast, for XD samples, all fibers align perpendicularly to the loading direction in the undeformed state. As the crack grows, most fibers do not reorient, neither participate in crack bridging, leading to the lowest traction (Fig. 8I and fig. S8B).

Effect of dehydration on the traction-separation curve

The bridging zone at the crack tip of the membrane forms by pullout of fibers. To investigate the effect of fiber pullout on the bridging behavior, we dehydrated the BP membrane. We fix both sides of the membrane with glass plates to ensure that the membrane remains flat during dehydration. Then, we place the membrane in an oven at a constant temperature of 50°C for 24 hours. After drying, the weight of the membrane is reduced by 80%, and the dehydrated membrane becomes optically transparent. The dehydration treatment makes the collagen molecules form more collagen-collagen hydrogen bonds rather than collagen-water hydrogen bonds; thus, the interfibrillar interaction increases (*42*, *43*) (Fig. 9A). Consequently, the slip and deformation of collagen fibers are constrained. When pulling out a fiber, the fiber is more likely to break rather than slip.

We conduct the crack growth experiment of the dehydrated membrane and observe the crack tip during the stretching process. When stretching the dehydrated membrane, the crack grows by fiber break (Fig. 9B). We observe the contours of strain E_{YY} around the crack tip using the digital image correlation method. The strain concentration at the crack tip of dehydrated BP is higher than that of fresh BP (Fig. 9C). The stronger interaction between fibers causes a shorter load transfer length for dehydrated BP, leading to the strain concentration at the crack tip (*44*). The stress-stretch curves are recorded, in which the dehydrated sample reaches the maximum stress at a small stretch. Both the modulus and maximum stress of dehydrated membrane are much higher than that of fresh membrane (fig. S12). We compare the function $G(\delta_t)$ for dehydrated and fresh membranes (Fig. 9D). The fibers in the dehydrated membrane break at a small separation of $\delta_t \sim 1.4$ mm. After fiber break, the crack grows steadily, and the energy release rate G reaches a plateau. When the separation is small, the energy release rate G of dehydrated membrane rises more quickly than that of fresh membrane. When the separation is large, G keeps growing for fresh membrane but stops growing for dehydrated membrane.

We compare G_A between fresh samples and dehydrated samples. G_A of the dehydrated sample is ~25 times lower than that of the fresh sample. Dehydration also decreases G_B obviously (Fig. 9E). The scanning electron microscope images show that, at the crack tip of the dehydrated BP, the fibers do not reorient completely. Instead, laminated crossover fibers bridge the crack surface in the bridging zone and some fibers are broken at the wake of the crack (fig. S13). Thus, G_A of the dehydrated sample is smaller. Because of the premature fiber breakage, the bridging zone at the crack tip is small; thus, G_B decreases.

We obtain the traction-separation curves for both the fresh BP and dehydrated BP (Fig. 9F). The peak traction is $\sigma_0 \sim 102$ MPa for dehydrated BP and $\sigma_0 \sim 63$ MPa for fresh BP (Fig. 9G). When stretching the dehydrated samples, fibers break due to the enhanced interaction between the fibers. For the same fiber length, fiber break can provide a larger bridging stress than fiber pullout. The dehydration decreases the maximum separation δ_0, from ~6.1 mm for fresh BP to ~1.4 mm for dehydrated BP. Because fibers break at the crack surface rather than being pulled out, the maximum separation of the dehydrated sample is much smaller than that of the fresh sample.

DISCUSSION

Crack bridging is ubiquitous in materials. On the plane of σ_0 and δ_0, we plot the data of soft tissues, hard tissues, and synthetic materials (*30*, *34*, *45*–*50*) (Fig. 10A). BP shows a high peak traction $\sigma_0 \sim 60$ MPa. This value is close to that of bone and nacre but much higher than that of unidirectional fiber/epoxy composite (*45*, *49*, *51*). The maximum separation $\delta_0 \sim 6$ mm of BP is among the highest in both biological tissues and synthetic materials. For nacre and bone, $\delta_0 \sim 10$ μm. For unidirectional fiber/epoxy composite, $\delta_0 \sim 1$ mm.

Crack bridging makes the BP flaw insensitive. The flaw insensitivity can be quantified by the fractocohesive length, defined as G_c/W_c (*52*, *53*). Here, W_c is the work of fracture, defined by the area under the stress-stretch curve of a sample without a precut crack (fig. S14). For BP, $W_c = 2.16 \times 10^3$ kJ/m^3. For applications that do not tolerate crack growth, we take G_c to be the critical value of the initiation of crack growth, $G_A \sim 15$ kJ/m^2. For applications that tolerate crack growth, we take G_c to be the critical value of the plateau of the energy release rate, $G_B \sim 108$ kJ/m^2. Using these values, the fractocohesive length of BP ranges from ~10 to ~50 mm. The fractocohesive length may explain the scale independent results in crack growth experiments of Fig. 7, where both the G_A, G_B, and the traction-separation curves do not depend on the sample height H when it approaches ~10 mm. On the plane of G_c and W_c, we plot the data of soft tissues,

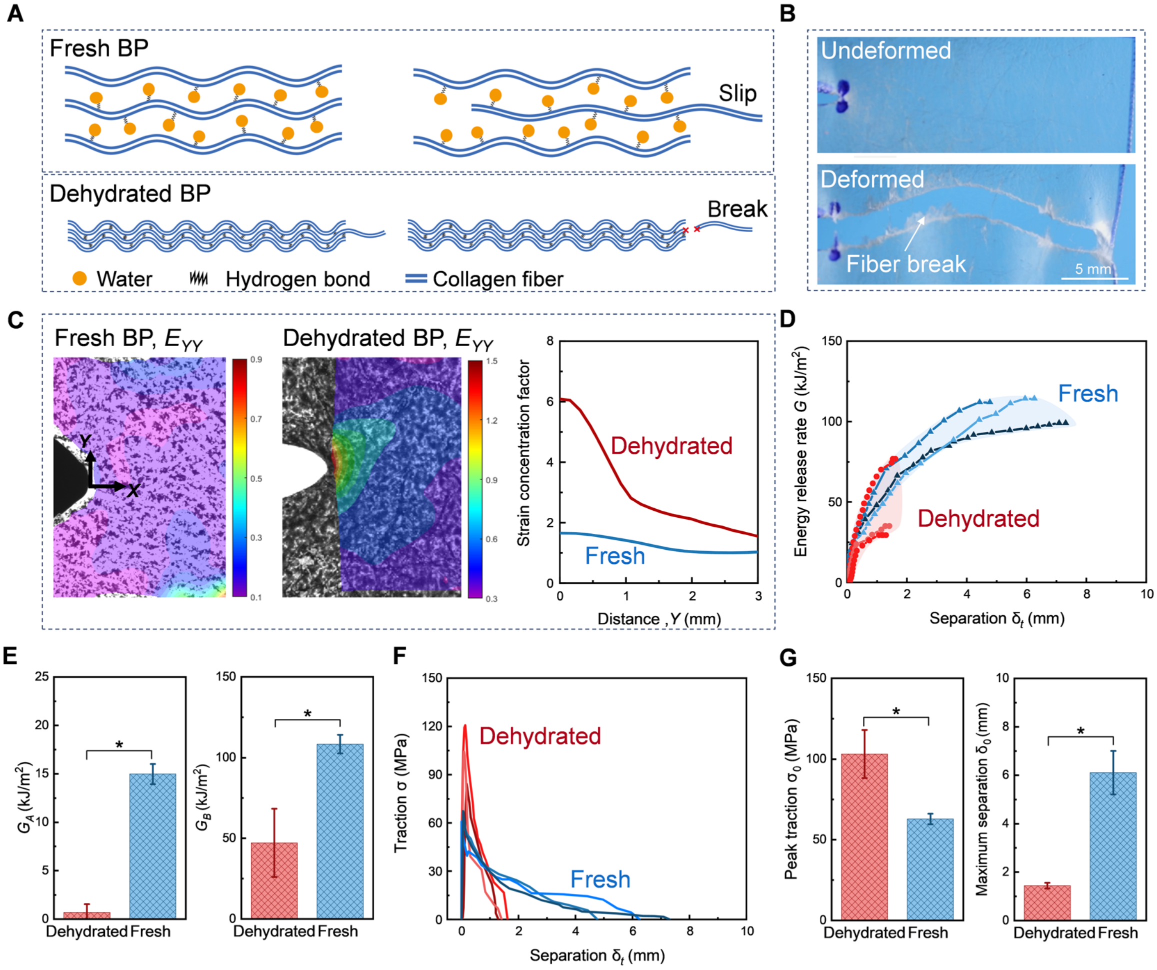

Fig. 9. Crack growth experiments using dehydrated samples. (**A**) When the membrane is dehydrated, hydrogen bonds form between collagens rather than between collagen and water. (**B**) Fiber breaks during the crack propagation in the dehydrated membrane. (**C**) Contours of strain E_{YY} and the strain concentration factor at distance Y from the crack tip measured in the undeformed state. (**D**) Energy release rate G as a function of crack separation δ_t. (**E**) Energy release rate at crack growth initiation, G_A, and the energy release rate at global failure, G_B. (**F**) Traction-separation curves and (**G**) the maximum traction σ_0 and the maximum separation δ_0 of fresh and dehydrated membranes. The sample height is fixed at 10 mm for all the tests, and the HD samples are used. The number of samples, $n = 3$, for both fresh samples and dehydrated samples. Significant differences ($P < 0.05$) are indicated by Student's t test.

hard tissues, and synthetic materials (*2*, *34*, *37*, *46*, *53*–*60*). Hard tissues (e.g., nacre and bone) show a much shorter fractocohesive length of ~1 mm (*56*, *58*–*60*). The work of fracture W_c of nacre is comparable to that of BP, but the toughness G_c of nacre is two orders of magnitude lower than that of BP. Thus, the fractocohesive length of nacre is two orders of magnitude shorter than that of BP. It is worthy to note that, for some soft collagenous tissues, such as rhinoceros dermis and aorta, collagen fibers may break during crack propagation. The break of collagen fibers also contributes to toughening these tissues (*61*, *62*). Furthermore, biological tissues also exhibit other toughening mechanisms at microscopic scales due to the hierarchical structure. For instance, the toughness of bones may stem from the action of sacrificial bonds and hidden length (*63*).

The crack bridging mechanism of various materials is compared (Fig. 10C). In the silica glass, each oxygen atom binds with two silicon atoms, and each silicon atom bonds four oxygen atoms. At a crack tip in the silica glass, the "bridging zone size" is limited to the atomic scale, on the order of 10^{-9} m. The toughness of silica glass is the bond energy per unit area in a single atomic layer, on the order of 10^{-3} kJ/m^2. For hard tissues like nacre, the crack growth involves the pullout of mineral platelets embedded in the protein-rich matrix. The length of the platelets is ~10 μm, and the bridging zone size is ~10^{-4} m. The toughness of nacre is ~1 kJ/m^2 (*34*). For BP, the bridging zone size is ~10^{-2} m, and the toughness reaches 100 kJ/m^2. For the unidirectional fiber/epoxy composite, crack grows in the fiber direction and is bridged by crossover fibers. The bridging zone size of the composites is ~1 m, with an interlaminar toughness of ~1 kJ/m^2 (*30*).

The architecture and microscopic processes of the BP membrane inform the development of biomimetic materials. As a replacement for human heart valves, BP usually does not fail by growing cracks but by calcification, so that such heart valves only last less than 10 years (*8*). This limitation has long motivated the development of BP-like synthetic materials (*64*). The reported synthetic materials do

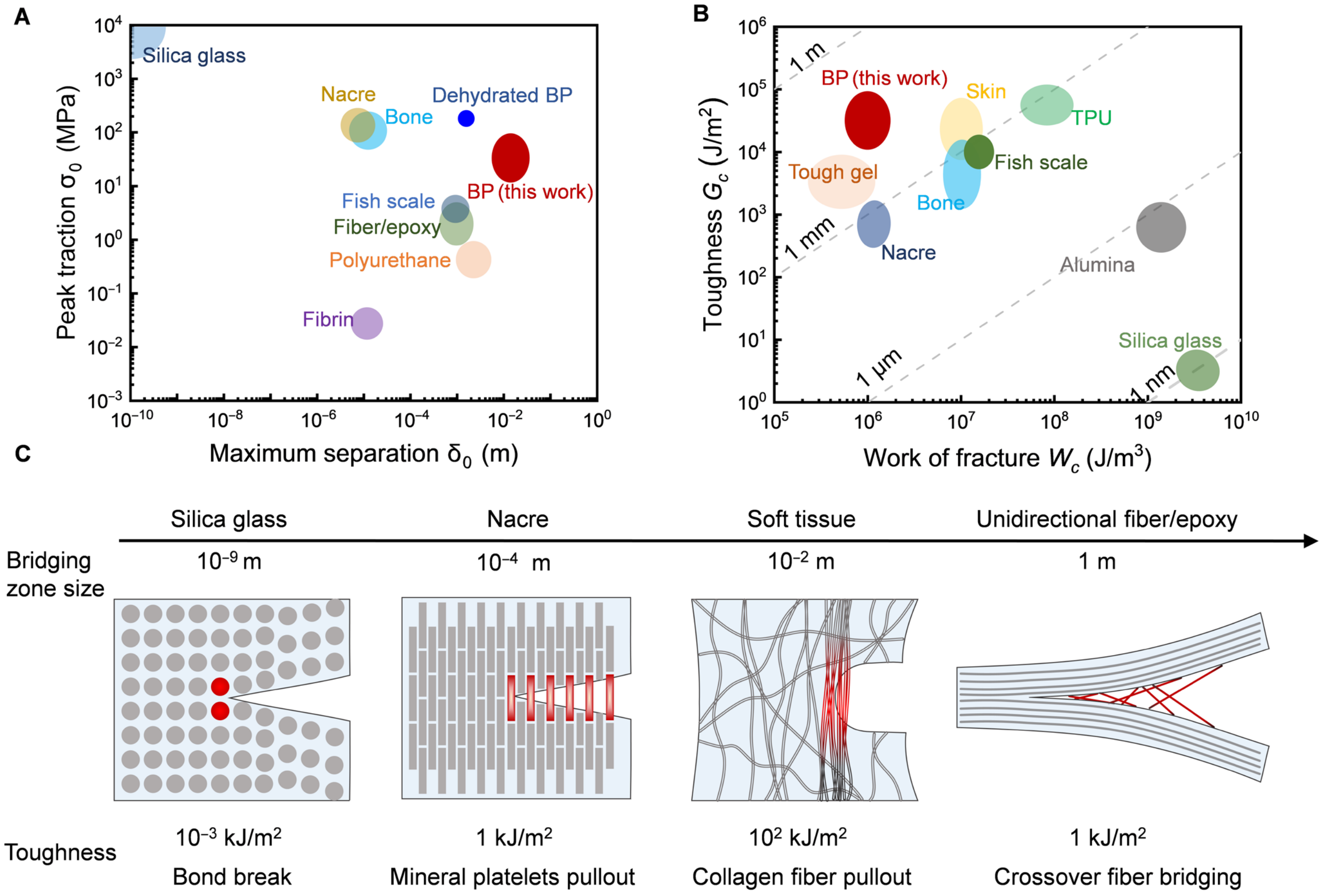

Fig. 10. Crack bridging in several materials. The materials are represented (**A**) on the plane of peak traction σ_0 and maximum separation δ_0 and (**B**) on the plane of toughness G_c and work of fracture W_c. The dashed lines denote the fractocohesive length G_c/W_c. (**C**) Bridging zone size and bridging mechanism of a few represented materials, including silica glass, nacre, soft collagenous tissue, and unidirectional fiber reinforced composite.

not match the toughness of BP. The materials need to fulfill two fundamental mechanical requirements: a low modulus to ensure opening and closing in pulsatile flow and a high crack resistance. The current study suggests a strategy to develop such materials by embedding a knitted fabric in a soft polymer matrix. The fibers need to be long and strong. When the stretch is small to modest, the knitted fabric is easily stretched, so that the composite is soft. When the stretch is large, the knitted fabric is stiff and strong. The soft matrix enables a fiber to transmit tension over a long length. We report this development elsewhere (*65*). In addition, future research can integrate existing constitutive relations of tissues with crack bridging model to predict the crack propagation of soft collagenous tissues under different loading conditions (*66*).

In this work, we investigate the origin of the high toughness of BP through mechanical tests and microscopic observations. We measure the traction-separation curve of BP using two methods: fiber pullout and crack growth. When pulling out from the matrix, the fibers decrimp and reorient, and the pullout length is ~10 mm. When stretching a sample with a precut crack, two values of energy release rate are identified, G_A and G_B. The crack starts to grow at G_A, and the sample undergoes global failure at G_B. We measure the energy release rate as a function of crack separation, $G(\delta_t)$, and convert this function to the traction-separation curve, $\sigma(\delta)$. The two methods give comparable traction-separation curves. The peak traction is σ_0 ~ 60 MPa, close to that of hard tissues. The maximum separation is δ_0 ~ 6 mm, two to four orders of magnitude higher than that of hard tissues. Both the high traction and large separation contribute to high toughness. The traction-separation curve does not change with the sample height but varies with the fiber orientation. The traction is the highest when the fibers align along the loading direction and is the lowest when the fibers align perpendicular to the loading direction. Moreover, we enhance the resistance to fiber pullout by dehydrating the membrane. After dehydration, the separation decreases but the traction increases due to the break of fibers at the crack surface. Lessons drawn from the biological tissue are expected to aid the development of synthetic materials.

MATERIALS AND METHODS

Materials

Fresh BP membrane is purchased from Maverick Biosciences Corporation (New South Wales, Australia) and supplied by courtesy of NewMed Medical Corporation (Shanghai, China). The tissue is harvested and transported to Maverick Biosciences Corporation within 24 hours of animal slaughter. After purchasing the pericardium, we store it in a refrigerator at 4°C until testing.

SALS test

We use the SALS test to nondestructively detect the orientation of collagen fibers (fig. S7). To increase the optical transparency, before the SALS test, the membrane is submerged sequentially in aqueous solutions of various concentrations of glycerol (20, 40, 60, 80, and 100%, twice) (*39*). The custom-designed SALS device consists of a He-Ne laser source (wavelength, 640 nm), a projecting screen, and a digital camera. The BP membrane has a square shape with dimensions of ~10 cm by 10 cm. The alignment of collagen fibers in the membrane may vary from region to region, so the membrane is divided into small square areas (2 cm by 2 cm). Then, the membrane is sandwiched between two glass plates. When the laser beam vertically passes through the membrane, a scattering pattern on the projecting screen reveals the orientation of fibers. A circular scattering pattern indicates that the fibers are not aligned, and an elliptical scattering pattern indicates that the fibers are highly aligned. Each small square area is detected, and the scattering patterns on the projecting screen are recorded using the digital camera.

Each scattering pattern is approximated by an ellipse, with eccentricity extracted using MATLAB. According to the eccentricity of each pattern, different parts of the membrane are sorted into two groups. The parts with the eccentricity below 0.5 are sorted into groups where collagen fibers are not aligned. The parts with the eccentricity over 0.7 are sorted into groups where collagen fibers are highly aligned (*67*). The fiber aligned direction coincides with the short axis of the elliptical scattering pattern. The BP membrane (10 cm by 10 cm) is stored in a refrigerator at 4°C after the SALS test. Before mechanical testing of samples, the BP membrane needs to be rehydrated using the aqueous solutions of glycerol (80, 60, 40, 20, and 0%, twice). Then, the prepared samples are soaked in deionized water for 12 hours to ensure complete rehydration. During testing, the samples are quickly taken out from the deionized water and tested immediately. A humidifier is used to prevent dehydration of the samples during the tests.

Multiphoton imaging

A sample is stretched and the displacement is held fixed by a loading frame (fig. S15). The membranes are placed between a glass slide and a glass coverslip. The sample, along with the frame and the glasses, is transferred into a multiphoton microscope (Leica SP8 DIVE) with a 25× objective lens immersed in water. The excitation wavelength is set at 820 nm to generate the two-photon excited fluorescence from elastin (520 to 550 nm) and the second harmonic generation from collagen (397 to 420 nm). The specimens are scanned from the top to the bottom in the thickness direction, capturing images of each layer at an increment of 5 μm.

Scanning electron microscopy

We use an acrylic frame to fix the sample with a certain stretch and then immerse the sample in 2.5% glutaraldehyde at 4°C for 24 hours to fix the microstructure of the membrane. The fixed membrane is then immersed in aqueous solution of ethanol solutions of ascending concentrations (20, 40, 60, 80, 90, and 100 wt %, twice) This process replaces water in the membrane with ethanol. The ethanol-soaked membranes are then dried in a dryer (Autosamdri-815A, Tousimis) for 24 hours. The dried samples are coated with platinum using a sputter coater (Hitachi MC1000) and observed in a scanning electron microscope (Hitachi SU3500).

Fiber pullout experiment

We prepare a rectangular sample with a width of 10 mm and a height of 30 mm. We cut the sample from two long edges in the middle plane and leave a ligament with a width of ~300 μm, containing a small number of collagen fibers (fig. S1A). The upper and lower edges of the sample are glued by acrylic sheets. The height of the acrylic sheet for the upper part is 10 mm, whereas that for the lower part is 5 mm. This setup ensures that collagen fibers in the upper part are totally fixed by the acrylic sheet and collagen fibers could only be pulled out from the lower part, facilitating observation and data recording. The sample is gripped by a tensile tester and pulled at a constant velocity of 20 mm/min (fig. S1B). To remove elastic deformation of the ligament from the displacement, we prepare an intact sample of the same size adjacent to the precut sample (fig. S1A). Both the intact sample and precut sample are stretched (fig. S1C). The force-displacement curves of the two samples are recorded (fig. S1, D and E). When the pullout force is F_a, the corresponding displacement for the precut sample is d_1, containing both the pullout length and elastic deformation. The elastic deformation is obtained from the force-displacement curve of the intact sample, by reading the displacement d_2 at the force F_a. We calculate the separation as $\delta_a = d_1 - d_2$. The traction σ_a is calculated by dividing the force by the initial cross-sectional area of the ligament $A_{ligament}$. Thus, we obtain the traction-separation curve by the fiber pullout experiment (fig. S1F). The resolution of the loading cell is 1×10^{-6} N. When the tensile tester detects a force of 0.001 N, we reset the force to zero, defining it as the initial state of all mechanical tests.

Crack growth experiment

We prepare a rectangular membrane with a width of 37.5 mm and a height of 22.5 mm, with a 15-mm precut crack introduced in the middle plane. The upper and lower edges of the sample are fixed to the acrylic sheet by the suture and glue. The sutures are used to fix the samples to the acrylic sheets, ensuring that they would not detach during the tensile tests. All samples are stretched by a tensile tester (Shimadzu AGS-X) at a speed of 20 mm/min with a load cell of 500 N. The nominal stress is calculated by dividing the force by the uncut cross-sectional area of the undeformed samples. For the crack growth experiment with different gauge heights of $H = 5$, 8, 13, and 15 mm, the total sample heights are 17.5, 20.5, 25.5, and 27.5 mm, respectively. All samples have a same width of 37.5 mm.

Uniaxial tension test

The dog bone–shaped samples (2 mm by 12 mm) are cut from the membrane where the fibers are not aligned. Samples are stretched by a tensile tester (Shimadzu AGS-X) at a speed of 20 mm/min with a load cell of 100 N. The stress-stretch curves are recorded. The nominal stress is calculated by dividing the force by the cross-sectional area of the undeformed sample. The stretch is defined by the current length of the sample divided by the length of the undeformed sample.

Digital image correlation method

We spray black paint on the surface of samples to obtain random speckles. As the sample is stretched, a digital camera is used to take images. The images are then analyzed by commercial software VIC-2D to extract the strain field.

Statistical analysis

Data are analyzed, fitted, and tested for statistical significance using commercial software IBM SPSS Statistics 24. The significance between more than two groups is analyzed with the Kruskal-Wallis test. The significance between two different groups is analyzed with a two-tailed Student's t test. P values of less than 0.05 are considered significant.

Supplementary Materials

The PDF file includes:

Figs. S1 to S15
Legends for movies S1 to S3

Other Supplementary Material for this manuscript includes the following:

Movies S1 to S3

REFERENCES AND NOTES

1. K. Bircher, M. Zündel, M. Pensalfini, A. E. Ehret, E. Mazza, Tear resistance of soft collagenous tissues. *Nat. Commun.* **10**, 792 (2019).
2. W. Yang, V. R. Sherman, B. Gludovatz, E. Schaible, P. Stewart, R. O. Ritchie, M. A. Meyers, On the tear resistance of skin. *Nat. Commun.* **6**, 6649 (2015).
3. L. Zeng, F. Liu, Q. Yu, C. Jin, J. Yang, Z. Suo, J. Tang, Flaw-insensitive fatigue resistance of chemically fixed collagenous soft tissues. *Sci. Adv.* **9**, eade7375 (2023).
4. X. Zhao, X. Chen, H. Yuk, S. Lin, X. Liu, G. Parada, Soft materials by design: Unconventional polymer networks give extreme properties. *Chem. Rev.* **121**, 4309–4372 (2021).
5. K. Bircher, A. E. Ehret, D. Spiess, M. Ehrbar, A. P. Simões-Wüst, N. Ochsenbein-Kölble, R. Zimmermann, E. Mazza, On the defect tolerance of fetal membranes. *Interface Focus* **9**, 20190010 (2019).
6. T. Ishihara, V. J. Ferrans, M. Jones, S. W. Boyce, W. C. Roberts, Structure of bovine parietal pericardium and of unimplanted Ionescu-Shiley pericardial valvular bioprostheses. *J. Thorac. Cardiovasc. Surg.* **81**, 747–757 (1981).
7. M. I. Ionescu, D. R. Smith, S. S. Hasan, M. Chidambaram, A. P. Tandon, Clinical durability of the pericardial xenograft valve: Ten years' experience with mitral replacement. *Ann. Thorac. Surg.* **34**, 265–277 (1982).
8. F. J. Schoen, R. J. Levy, Tissue heart valves: Current challenges and future research perspectives. *J. Biomed. Mater. Res.* **47**, 439–465 (1999).
9. M. Kütting, J. Roggenkamp, U. Urban, T. Schmitz-Rode, U. Steinseifer, Polyurethane heart valves: Past, present and future. *Expert Rev. Med. Devices* **8**, 227–233 (2011).
10. I. Vesely, The role of elastin in aortic valve mechanics. *J. Biomech.* **31**, 115–123 (1997).
11. M. Asgari, N. Latifi, H. K. Heris, H. Vali, L. Mongeau, In vitro fibrillogenesis of tropocollagen type III in collagen type I affects its relative fibrillar topology and mechanics. *Sci. Rep.* **7**, 1392 (2017).
12. J. P. R. O. Orgel, J. D. San Antonio, O. Antipova, Molecular and structural mapping of collagen fibril interactions. *Connect. Tissue Res.* **52**, 2–17 (2011).
13. M. J. Buehler, Nature designs tough collagen: Explaining the nanostructure of collagen fibrils. *Proc. Natl. Acad. Sci. U.S.A.* **103**, 12285–12290 (2006).
14. W. M. Han, N. L. Nerurkar, L. J. Smith, N. T. Jacobs, R. L. Mauck, D. M. Elliott, Multi-scale structural and tensile mechanical response of annulus fibrosus to osmotic loading. *Ann. Biomed. Eng.* **40**, 1610–1621 (2012).
15. M. Sharabi, Structural mechanisms in soft fibrous tissues: A review. *Front. Mater.* **8**, 793647 (2022).
16. A. S. Craig, M. J. Birtles, J. F. Conway, D. A. D. Parry, An estimate of the mean length of collagen fibrils in rat tail-tendon as a function of age. *Connect. Tissue Res.* **19**, 51–62 (1989).
17. B. E. Peterson, S. E. Szczesny, Dependence of tendon multiscale mechanics on sample gauge length is consistent with discontinuous collagen fibrils. *Acta Biomater.* **117**, 302–309 (2020).
18. M. A. Meyers, P.-Y. Chen, A. Y.-M. Lin, Y. Seki, Biological materials: Structure and mechanical properties. *Prog. Mater. Sci.* **53**, 1–206 (2008).
19. E. Gentleman, A. N. Lay, D. A. Dickerson, E. A. Nauman, G. A. Livesay, K. C. Dee, Mechanical characterization of collagen fibers and scaffolds for tissue engineering. *Biomaterials* **24**, 3805–3813 (2003).
20. H. Miyazaki, K. Hayashi, Tensile tests of collagen fibers obtained from the rabbit patellar tendon. *Biomed. Microdevices* **2**, 151–157 (1999).
21. X. Yu, B. Suki, Y. Zhang, Avalanches and power law behavior in aortic dissection propagation. *Sci. Adv.* **6**, eaaz1173 (2020).
22. H. Oxlund, J. Manschot, A. Viidik, The role of elastin in the mechanical properties of skin. *J. Biomech.* **21**, 213–218 (1988).
23. S. Rigozzi, R. Müller, A. Stemmer, J. G. Snedeker, Tendon glycosaminoglycan proteoglycan sidechains promote collagen fibril sliding-AFM observations at the nanoscale. *J. Biomech.* **46**, 813–818 (2013).
24. A. Pissarenko, W. Yang, H. Quan, B. Poyer, A. Williams, K. A. Brown, M. A. Meyers, The toughness of porcine skin: Quantitative measurements and microstructural characterization. *J. Mech. Behav. Biomed. Mater.* **109**, 103848 (2020).
25. K. Stok, A. Oloyede, A qualitative analysis of crack propagation in articular cartilage at varying rates of tensile loading. *Connect. Tissue Res.* **44**, 109–120 (2003).
26. S. N. S. H. Chittajallu, H. Gururani, K. M. Tse, S. N. Rath, S. Basu, V. Chinthapenta, Investigation of microstructural failure in the human cornea through fracture tests. *Sci. Rep.* **13**, 13876 (2023).
27. G. I. Barenblatt, The formation of equilibrium cracks during brittle fracture. General ideas and hypotheses. Axially-symmetric cracks. *J. Appl. Math. Mech.* **23**, 622–636 (1959).
28. D. S. Dugdale, Yielding of steel sheets containing slits. *J. Mech. Phys. Solids* **8**, 100–104 (1960).
29. A. Needleman, A continuum model for void nucleation by inclusion debonding. *J. Appl. Mech.* **54**, 525–531 (1987).
30. G. Bao, Z. Suo, Remarks on crack-bridging concepts. *Appl. Mech. Rev.* **45**, 355–366 (1992).
31. S. Li, M. Thouless, A. Waas, J. Schroeder, P. Zavattieri, Use of a cohesive-zone model to analyze the fracture of a fiber-reinforced polymer–matrix composite. *Compos. Sci. Technol.* **65**, 537–549 (2005).
32. B. N. Cox, D. B. Marshall, Concepts for bridged cracks in fracture and fatigue. *Acta Metall. Mater.* **42**, 341–363 (1994).
33. H. Yao, H. Gao, Multi-scale cohesive laws in hierarchical materials. *Int. J. Solids Struct.* **44**, 8177–8193 (2007).
34. Y. Shao, H.-P. Zhao, X.-Q. Feng, H. Gao, Discontinuous crack-bridging model for fracture toughness analysis of nacre. *J. Mech. Phys. Solids* **60**, 1400–1419 (2012).
35. V. R. Sherman, W. Yang, M. A. Meyers, The materials science of collagen. *J. Mech. Behav. Biomed. Mater.* **52**, 22–50 (2015).
36. S. M. Mijailovich, D. Stamenović, J. J. Fredberg, Toward a kinetic theory of connective tissue micromechanics. *J. Appl. Physiol.* **74**, 665–681 (1993).
37. R. S. Rivlin, A. G. Thomas, Rupture of rubber. I. Characteristic energy for tearing. *J. Polym. Sci.* **10**, 291–318 (1953).
38. J. R. Rice, A path independent integral and the approximate analysis of strain concentration by notches and cracks. *J. Appl. Mech.* **35**, 379–386 (1968).
39. M. S. Sacks, D. B. Smith, E. D. Hiester, A small angle light scattering device for planar connective tissue microstructural analysis. *Ann. Biomed. Eng.* **25**, 678–689 (1997).
40. J. Tang, J. Lin, T. Wang, Cracking of soft collagenous tissues under suture retention. *J. Mech. Phys. Solids* **188**, 105682 (2024).
41. A. Whelan, J. Duffy, R. T. Gaul, D. O'Reilly, D. R. Nolan, P. Gunning, C. Lally, B. P. Murphy, Collagen fibre orientation and dispersion govern ultimate tensile strength, stiffness and the fatigue performance of bovine pericardium. *J. Mech. Behav. Biomed. Mater.* **90**, 54–60 (2019).
42. A. Gautieri, S. Vesentini, A. Redaelli, M. J. Buehler, Viscoelastic properties of model segments of collagen molecules. *Matrix Biol.* **31**, 141–149 (2012).
43. S. Bose, S. Li, E. Mele, V. V. Silberschmidt, Fracture behaviour and toughening mechanisms of dry and wet collagen. *Acta Biomater.* **142**, 174–184 (2022).
44. J. M. Hedgepeth, *Stress Concentrations in Filamentary Structures* (National Aeronautics and Space Administration, 1961).
45. A. G. Evans, Z. Suo, R. Z. Wang, I. A. Aksay, M. Y. He, J. W. Hutchinson, Model for the robust mechanical behavior of nacre. *J. Mater. Sci. Res.* **16**, 2475–2484 (2001).
46. A. Khayer Dastjerdi, F. Barthelat, Teleost fish scales amongst the toughest collagenous materials. *J. Mech. Behav. Biomed. Mater.* **52**, 95–107 (2015).
47. R. O. Ritchie, J. H. Kinney, J. J. Kruzic, R. K. Nalla, A fracture mechanics and mechanistic approach to the failure of cortical bone. *Fatigue Fract. Eng. Mater. Struct.* **28**, 345–371 (2005).
48. R. K. Nalla, J. S. Stölken, J. H. Kinney, R. O. Ritchie, Fracture in human cortical bone: Local fracture criteria and toughening mechanisms. *J. Biomech.* **38**, 1517–1525 (2005).
49. B. F. Sørensen, T. K. Jacobsen, Determination of cohesive laws by the J integral approach. *Eng. Fract. Mech.* **70**, 1841–1858 (2003).
50. A. Khayer Dastjerdi, E. Tan, F. Barthelat, Direct measurement of the cohesive law of adhesives using a rigid double cantilever beam technique. *Exp. Mech.* **53**, 1763–1772 (2013).
51. B. F. Sørensen, T. K. Jacobsen, Large-scale bridging in composites: R-curves and bridging laws. *Compos. Part A Appl. Sci. Manuf.* **29**, 1443–1451 (1998).
52. A. Thomas, Rupture of rubber. II. The strain concentration at an incision. *J. Polym. Sci.* **18**, 177–188 (1955).
53. C. Chen, Z. Wang, Z. Suo, Flaw sensitivity of highly stretchable materials. *Eetreme Mech. Lett.* **10**, 50–57 (2017).
54. J.-Y. Sun, X. Zhao, W. R. Illeperuma, O. Chaudhuri, K. H. Oh, D. J. Mooney, J. J. Vlassak, Z. Suo, Highly stretchable and tough hydrogels. *Nature* **489**, 133–136 (2012).
55. C. H. Yang, M. X. Wang, H. Haider, J. H. Yang, J.-Y. Sun, Y. M. Chen, J. Zhou, Z. Suo, Strengthening alginate/polyacrylamide hydrogels using various multivalent cations. *ACS Appl. Mater. Interfaces* **5**, 10418–10422 (2013).

56. S. Alghamdi, F. Du, J. Yang, G. Pinder, T. Tan, Tensile and shear behavior of microscale growth layers between nacre in red abalone. *J. Mech. Phys. Solids* **138**, 103928 (2020).
57. U. G. Wegst, M. F. Ashby, The mechanical efficiency of natural materials. *Philos. Mag.* **84**, 2167–2186 (2004).
58. T. L. Norman, D. Vashishth, D. B. Burr, Fracture toughness of human bone under tension. *J. Biomech.* **28**, 309–320 (1995).
59. H. S. Gupta, P. Zioupos, Fracture of bone tissue: The 'hows' and the 'whys'. *Med. Eng. Phys.* **30**, 1209–1226 (2008).
60. C.-Y. Lin, J.-H. Kang, Mechanical properties of compact bone defined by the stress-strain curve measured using uniaxial tensile test: A concise review and practical guide. *Materials* **14**, 4224 (2021).
61. C. Miller, T. C. Gasser, A bottom-up approach to model collagen fiber damage and failure in soft biological tissues. *J. Mech. Phys. Solids* **169**, 105086 (2022).
62. R. E. Shadwick, A. P. Russell, R. F. Lauff, The structure and mechanical design of rhinoceros dermal armour. *Philos. Trans. R. Soc. London Ser. B Biol. Sci.* **337**, 419–428 (1992).
63. G. E. Fantner, T. Hassenkam, J. H. Kindt, J. C. Weaver, H. Birkedal, L. Pechenik, J. A. Cutroni, G. A. G. Cidade, G. D. Stucky, D. E. Morse, P. K. Hansma, Sacrificial bonds and hidden length dissipate energy as mineralized fibrils separate during bone fracture. *Nat. Mater.* **4**, 612–616 (2005).
64. D. Bezuidenhout, D. F. Williams, P. Zilla, Polymeric heart valves for surgical implantation, catheter-based technologies and heart assist devices. *Biomaterials* **36**, 6–25 (2015).
65. X. Chen, F. Liu, Q. Yu, M. Yang, Z. Suo, J. Tang, A soft and fatigue-resistant material that mimics heart valves. *Matter* **8**, 101926 (2025).
66. V. R. Sherman, Y. Tang, S. Zhao, W. Yang, M. A. Meyers, Structural characterization and viscoelastic constitutive modeling of skin. *Acta Biomater.* **53**, 460–469 (2017).
67. R. T. Gaul, D. R. Nolan, C. Lally, Collagen fibre characterisation in arterial tissue under load using SALS. *J. Mech. Behav. Biomed. Mater.* **75**, 359–368 (2017).

Acknowledgments: We acknowledge the support from the Instrumental Analysis Center of Xi'an Jiaotong University for facility support. We would like to thank Shanghai NewMed Medical Co. Ltd. (China) for providing the BP membranes. **Funding:** This research was supported by the National Natural Science Foundation of China (grant no. 12422204). Jingda Tang acknowledges the support of K. C. Wong Education Foundation. **Author contributions:** Conceptualization: Jingyuan Tang, L.Z., Z.S., and Jingda Tang. Methodology: Jingyuan Tang, X.C., F.L., Z.S., and Jingda Tang. Formal analysis and investigation: Jingyuan Tang, X.C., F.L., Z.S., and Jingda Tang. Writing—original draft preparation: Jingyuan Tang and Jingda Tang. Writing—review and editing: Z.S. and Jingda Tang. Supervision: Z.S. and Jingda Tang. **Competing interests:** The authors declare that they have no competing interests. **Data and materials availability:** All data needed to evaluate the conclusions in the paper are present in the paper and/or the Supplementary Materials.

Submitted 22 January 2025
Accepted 13 May 2025
Published 18 June 2025
10.1126/sciadv.adw0808